ACS APPLIED MATERIALS & INTERFACES

Article

Anti-IL8/AuNPs–rGO/ITO as immunosensing platform for non-invasive electrochemical detection of oral cancer

Shilpi Verma, Anu Singh, Ajay K. Shukla, Jyoti Kaswan, Kavita Arora, Jaime Ramirez-Vick, Priti Singh, and Surinder P Singh

ACS Appl. Mater. Interfaces, **Just Accepted Manuscript** • DOI: 10.1021/acsami.7b06839 • Publication Date (Web): 02 Aug 2017

Just Accepted

ACS Publications

ACS Applied Materials & Interfaces is published by the American Chemical Society.
1155 Sixteenth Street N.W., Washington, DC 20036

Anti-IL8/AuNPs–rGO/ITO as immunosensing platform for non-invasive electrochemical detection of oral cancer

Shilpi Verma,[1,3] Anu Singh,[2] Ajay Shukla,[3] Jyoti Kaswan,[1,3] Kavita Arora,[2] Jaime Ramirez-Vick,[4] Priti Singh,[3] Surinder P. Singh,*[1,3]*

[1]Academy of Scientific and Innovative Research (AcSIR), CSIR-National Physical Laboratory (NPL), Dr. K. S. Krishnan Road,

New Delhi-110012, India

[2]Advanced Instrumentation Research Facility (AIRF), Jawaharlal Nehru University (JNU), New Mehrauli Road, New Delhi-110067, India

[3]CSIR-National Physical Laboratory (NPL), Dr. K. S. Krishnan Road, New Delhi-110012, India

[4]Department of Biomedical, Industrial & Human Factors Engineering, Wright State University, Dayton, OH 45435, USA

KEYWORDS: Immunosensor, reduced graphene oxide, gold nanoparticles, cyclic voltammetry, electrochemical biosensor, interleukin-8

ABSTRACT

The efficient electrochemical transducer matrix for biosensing devices requires specific characteristics of fast electron transfer, stability, high surface area, biocompatibility and presence of specific functional groups facilitating for biomolecule attachment. We demonstrate the fabrication of an electrochemical immunosensor based on highly stable gold nanoparticles-reduced graphene oxide (AuNPs-rGO) composite material as transducer matrix for label-free and non-invasive detection of salivary oral cancer biomarker interleukin-8 (IL8). The synergy between rGO and AuNPs allowed the immunosensor to exhibit fast response and high sensitivity due to the improved electron transfer behavior of the composite. The immunosensor shows very fast detection (9 min) of IL8 and high sensitivity with experimental linear dynamic range of 500 fg mL^{-1} to 4 ng mL^{-1} and detection limit of 72.73±0.18 pg mL^{-1}. The fabricated immunosensor exhibits excellent specificity towards detection of IL8 in the human saliva samples. Furthermore, the reusability and stability up to three months of the immunosensor demonstrates the commercial potential of this nanoplatform for the detection of other biomarkers of clinical relevance.

1. INTRODUCTION

Head and neck cancer is a broad term that encompasses epithelial malignancies that arise in the mucosal surfaces of paranasal sinuses, nasal cavity, oral cavity, oropharynx, and larynx, with more than 90% occurring on the last three sites, which can be classified as oral cancer.[1,2] Due to its high global pervasiveness, oral cancer has been identified to be a major global health concern.[3-5] The American Cancer Society estimates 49,670 new cases and 9,700 deaths due to oral cancer during 2017 in the United States.[6] Despite of excellent developments in diagnostic

and therapeutic modalities for oral cancer the survival rate is still low. One of the major causes for the failure of treatment modalities is late diagnosis of the disease. Existing diagnostic techniques (e.g. brush biopsy, cytopathology, visualization adjuncts etc.) are not able to detect the disease until it reaches the advanced stage.[7,8] The development of sensitive point-of-care screening techniques for early stage diagnosis of oral cancer can largely contribute to increased therapeutic efficiency, resulting in a decrease in mortality rate from this dreadful disease.

Cancer biomarkers are specific class of biological substances (such as DNA, mRNA, proteins, enzymes) whose expression in body fluids, cells or tissues correlate with the malignant condition.[9] Real-time quantitative monitoring of these biomarkers is essential for early detection of the disease, directing personalized treatments and analysis of treatment efficacy.[10] Interleukin-8 (IL8), is a cytokine, associated with the angiogenic and mitotic processes in various types of cancers.[11,12] Researchers have discovered elevated expression levels of IL8 in saliva of oral cancer patients (i.e. 720 pg mL^{-1}) compared to those found in control group (i.e. 250 pg mL^{-1}).[13] Monitoring IL8 in saliva of patients with suspected oral cancer can therefore pave the way for early detection of oral cancer through non-invasive sampling, making it an important diagnostic tool of clinical value. Conventional methods used for measurement of biomarkers include enzyme-linked immunosorbent assay (ELISA), gel electrophoresis, mass spectrometry, fluorescence assay and surface enhanced Raman spectroscopy. Although these technologies provide accurate and reliable results, limitations such as, detection time, sample amount, sensitivity, equipment cost and requirement of highly trained user, make them poor alternatives for clinical applications.[14,15]

The use of electrochemical immunosensing for quantifying biomarkers has proven to be a simple, speedy, cost-effective and portable monitoring method for clinical diagnosis.[16-17]

However, development of sensitive and accurate electrochemical biosensing systems relies on choosing of bioreceptor and transducer matrices that are robust, biocompatible, provide high surface-to-volume ratio, are electrochemically active, and have a high electron transfer rate. Recently, many reports have shown application of nanomaterials like CNTs, metal nanoparticles, polymeric nanomaterials, magnetic nanoparticles and nano-hybrids in electrode fabrication which greatly enhance the electrochemical performance of the immunosensors.[18-20] Graphene oxide (GO) has emerged as an attractive matrix material for biosensing applications due to its two-dimensional structure, mechanical stability, biocompatibility and with electronic properties that can be easily tuned.[21]. Moreover, GO with oxygen containing functional groups, specifically –COOH allows for simple covalent binding of biomolecules (e.g. antibodies) at the surface without introduction of a linker molecule. Furthermore, metal nanoparticles can be incorporated onto GO to form a composite, which allows the modulation of the electronic and electrochemical properties of the composite to improve signal amplification and measurement time, to optimize biosensing applications.[22]

In the present work, a customized AuNPs-rGO nanocomposite based bioelectrode has been fabricated for the sensitive and label-free *point-of-care* detection of oral cancer biomarker IL8 from saliva. The immunosensor has been designed using the well characterized AuNPs-rGO nanocomposites as thin films on Indium tin oxide (ITO) coated glass followed by immobilization of anti-IL8 antibodies (as receptors) through covalent bonding between the amine group of antibodies and carboxylic group of rGO on the electrode surface. Successful immobilization was confirmed by techniques like Fourier Transform Infrared Spectroscopy (FTIR), X-ray photoelectron spectroscopy (XPS), Atomic Force Microscopy (AFM) and Cyclic Voltammetry (CV). The standardization of the immunosensor was done by measuring different concentrations

of IL8 antigen by Differential Pulse Voltammetry (DPV). Moreover, the immunosensor was successfully tested for detection of IL8 in spiked saliva samples. The immunosensor showed enhanced sensitivity and specificity within a wide linearity range. The improved electrochemical activity of the immunosensor is attributable to the efficient charge transfer mechanism provided by the AuNPs-rGO nanocomposite transducer matrix.

2. EXPERIMENTAL SECTION

2.1 Chemicals and Materials. All the chemicals were used as received. Graphite was bought from Acros Organics. Sodium nitrate ($NaNO_3$), hydrogen peroxide (H_2O_2), potassium permanganate ($KMnO_4$), potassium chloride (KCl), sodium chloride (NaCl), trisodium citrate ($Na_3C_6H_5O_7$) were purchased from Merck. Sulfuric acid (H_2SO_4), Gold(III) chloride hydrate ($HAuCl_4$), N-Ethyl-N′-(3-dimethylaminopropyl) carbodiimide hydrochloride (EDC), N-hydroxysuccinimide (NHS), sodium phosphate dibasic dehydrate ($Na_2HPO_4.2H_2O$), potassium phosphate monobasic (KH_2PO_4), potassium hexacyanoferrate(II) trihydrate ($K_4Fe(CN)_6.3H_2O$), potassium hexacyanoferrate(III) ($K_3Fe(CN)_6$) and ethanolamine ($HOCH_2CH_2NH_2$) were purchased from Sigma-Aldrich. ITO glass substrates (glass thickness: 1mm, coating thickness: 1500Å, resistivity: 15-20 Ω.cm) were obtained from Macwin India. IL8 antigen and IL8 rabbit polyclonal antibodies were procured from Bioss USA. Milli-Q water with resistivity of 18 MΩ.cm was used to prepare or dilute the buffers and various reagents used in the experiment.

2.2 Synthesis of Graphene Oxide. Graphene oxide was synthesized (**Scheme 1a**) using modified Hummer's method.[23] Briefly, 0.5 g of graphite and 0.5 g of $NaNO_3$ in 23 mL H_2SO_4 (98%) were kept at continuous stirring in ice bath (0-5 ºC). Finely powdered $KMnO_4$ (1.5 g) was

then slowly added to the reaction mixture under stirring, until it turned to dark green color. After 1 h the solution was transferred to water bath maintained at 35-40 ºC and stirred for another hour. Thereafter, 100 mL of deionized water was added through a funnel along the sides of the flask, yielding a dark brown solution. This solution was then sonicated for 30 min followed by the addition of 1 mL H_2O_2 (30%) upon which the solution turned yellow indicating the termination of reaction. The solution was then centrifuged and washed with deionized water several times until the pH of the GO solution became neutral. The neutral GO solution was finally lyophilized to attain a highly exfoliated, yellow colored, dry, fluffy GO powder.

2.3 Synthesis of AuNPs-rGO nanocomposite. AuNPs-rGO nanocomposite was prepared (**Scheme 1b**) using the method given by J. Song et al.[24] with slight modifications in the precursor concentrations and reaction conditions. The optimized process involves addition of 1 mL of a 25 mM $HAuCl_4$ solution to 50 mL of a well dispersed 0.1 mg mL^{-1} solution of GO in deionized water (0.1 mg mL^{-1}) under stirring. The uniform dispersion and fastening of Au^{3+} ions on the GO sheets was achieved by initially stirring the solution for 15 min and then keeping it undisturbed for 30 min. Then, 5 mL of 44 mM trisodium citrate was added and then refluxed for 30 min. The reddish-brown solution that formed was removed from heating, cooled and then centrifuged at 7000 rpm for 30 min to remove any unbound precursors. The pellet obtained was re-dispersed in 2 mL deionized water and lyophilized.

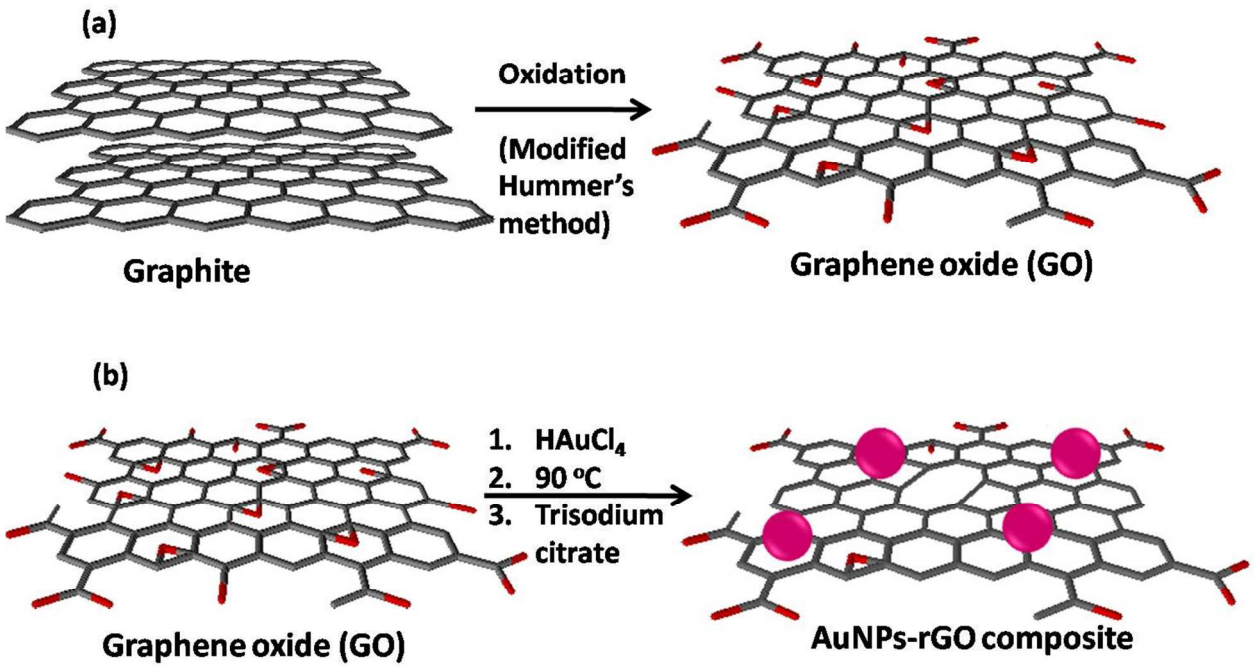

Scheme 1. Schematics of (a) formation of GO from graphite (b) *in-situ* synthesis of AuNPs-rGO nanocomposites.

2.4 Fabrication of Anti-IL8/AuNPs-rGO/ITO immunoelectrode. ITO coated glass of 10×5 mm^2 was used for surface modification towards immunoelectrode fabrication. Prior to use, ITO was sequentially cleaned by sonication in detergent, acetone, ethanol and deionized water. Thin films of 0.5 mg/mL solutions of GO and AuNPs-rGO on ITO were made using a programmable spin coater (Laurel 650). The films were annealed at 100 ºC for 3 h. These films were then treated with 40 µL of 1:1 mixture of 0.5 M EDC and 0.1 M NHS for 30 minutes for –COOH group activation. Then 20 µL of anti-IL8 antibodies were immobilized onto the activated film surface for 3 h. Unbound antibodies were removed by washing the films with 10 mM phosphate buffered saline (PBS). A 1 M ethanolamine solution was used to block the remaining active sites and the resulting immunoelectrode was then washed with 10 mM PBS. **Scheme 2** represents the procedure for the fabrication of the immunoelectrode. The prepared GO/ITO and AuNPs-rGO/ITO electrodes were characterized using different spectroscopic techniques and their

electrochemical activities were studied using CV. The CV was performed using a three-electrode-system in 3 mM Zobell's solution against Ag/AgCl as reference electrode and platinum as counter electrode.

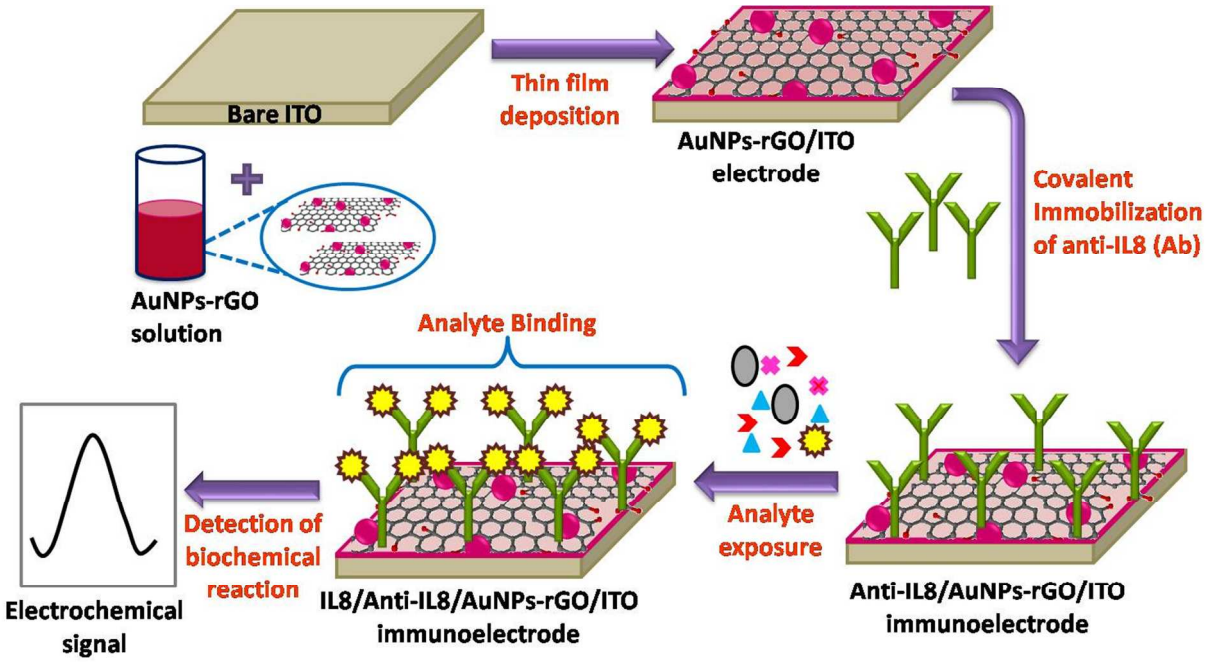

Scheme 2. Schematic of fabrication of AuNPs-rGO based immunoelectrode for immunosensing application.

2.5 Analyte (IL8) Sample Preparation. Different concentrations of IL8 (ranging from 500 fg/mL to 50 ng/mL) were prepared in 10 mM PBS (pH 7.4) and applied on the surface of the immunoelectrodes for 9 min. The resulting immunoreactions were studied using DPV technique in 1:1 v/v ratio of 10 mM PBS and 3 mM Zobell's solution at scan rate of 0.02 Vs^{-1} with pulse potential and pulse time values of 0.02 V and 0.07 s, respectively.

This fabricated immunosensor was tested for real sample analysis by spiking IL8 in control saliva. The control saliva sample was centrifuged at 8000 rpm for 15 min to remove any food

particles or residues and the clear supernatant was collected for further use. This saliva sample (without any dilution) was spiked with different concentrations of IL8 and the binding on Anti-IL8/AuNPs-rGO/ITO immunoelectrodes was studied using DPV.

2.6 Physical Characterizations. FTIR spectra of the compounds were obtained on Agilent Cary 360 FTIR in the range of 3600 to 400 cm^{-1} in ATR mode. UV-Visible spectra were recorded in the range 200 to 800 nm using Agilent Cary 5000 UV-Vis-NIR. Raman spectra were taken using Ranishaw win-via reflex spectrometer in the range of 200 to 2000 cm^{-1} with excitation source of Nd:Yag laser having 514 nm wavelength. XRD patterns were measured on Rigaku miniflex 300 bench top X-Ray Diffractometer consisting of Cu α radiation (λ = 1.541 Å). TEM images were acquired using Tecnai G2 F30 STWIN in conjunction with field emission electron source working at the electron accelerating voltage of 300 kV. The samples were dropcasted on carbon-coated copper grid (200 mesh) and kept for drying at room temperature. Solutions of GO and AuNPs-rGO were deposited on ITO coated glass plates (10 × 5 mm^2) using spin coater at (model: WS-650MZ-23NPP) 3000 rpm with acceleration 500 for 2 min. AFM images were taken in tapping mode using a Veeco V Atomic Force Microscope Nanoscope. XPS measurements were performed in an ultra-high vacuum multi chamber system using monochromatic Al Kα x-ray source and high resolution electron energy analyzer from Omicron GmbH. All the core level data were acquired using 20 eV pass energy and overall energy resolution of the spectrometer is estimated to be 0.4 eV. Binding energies are referenced to the Fermi edge of clean Ag foil. Shirley background subtraction was performed for all the core level data. Electrochemical studies were conducted using PalmSens3 instrument assisted with a three electrode cell system comprising of a Ag/AgCl reference electrode, Pt mesh counter electrode and GO or AuNPs-rGO deposited ITO coated glass plates as working electrode. Electrochemical

Impedance Spectroscopy (EIS) measurements were recorded at potential of 0.2 V in the frequency range of 0.1 Hz to 100 kHz using Metrohm Autolab.

3. RESULTS AND DISCUSSION

The structural and optical properties of the synthesized GO and AuNPs-rGO, observed by various techniques show the formation of both materials. X-ray diffraction patterns of graphite, GO and AuNPs-rGO are shown in **Figure 1a**. The diffraction pattern of graphite shows a very sharp diffraction peak at 2θ value of 26.4º with the interplanar distance of 3.38 Å.[25,26] The XRD of GO exhibits a distinct high intensity peak at 2θ value of 9.9º corresponding to (002) plane with interplanar spacing of 8.96 Å.[25,27,28] XRD of AuNPs-rGO revealed the presence of diffraction peaks at 2θ = 38.4, 44.4, 64.7 and 77.3º corresponding to (111), (200), (220) and (311) diffraction planes of fcc metallic gold (JCPDS no. 4-0784)[26,28] and a broad peak for (002) plane of disordered structure of rGO at 2θ = 22.6º.[25,29] FTIR spectroscopy has been used to corroborate the conversion of graphite to GO (**Figure 1b**). A broad band related to O-H stretching of various hydroxyl groups in GO was seen at 3247 cm^{-1}. C=O stretch was observed at 1720 cm^{-1} confirming the presence of carboxylic groups while C=C stretch corresponding to the sp^2 carbon network was observed at 1623 cm^{-1}. Peaks related to C-O stretching of carboxyl, epoxy and alkoxy group of GO were found at 1413, 1227 and 1057 cm^{-1} wavenumbers.[27,30] The FTIR spectrum of AuNPs-rGO (**Figure 1b**) also shows all the characteristic peaks related to GO, but the intensities of O-H stretch and epoxy C-O stretch have decreased significantly as compared to that in GO and the intensity of C=C stretch has increased with a minor shift of wavenumber. The variation in IR intensities is attributed to the partial reformation of C=C

network in AuNPs-rGO composite due to the reduction of GO during the synthesis process. The optical properties of GO and AuNPs-rGO were explored using UV-visible spectroscopy as can be seen in **Figure 1c**. The UV-visible spectrum of GO displayed the characteristic bands of π-π* (229 nm) and n-π* (300 nm) transitions.[31,32] Comparatively, weaker absorptions for similar transitions (i.e. π-π* transition at 236 nm and n-π* transition at 302 nm) were observed in the UV-visible spectrum of AuNPs-rGO, indicating removal of some of the functional groups in the composite. This spectrum also exhibited a broad surface plasmon resonance band at 530 nm pertaining to the formation of gold nanoparticles onto GO sheets.[33] **Figure 1d**, shows the Raman spectra of GO and AuNPs-rGO. The presence of D-band related to defects induced breathing mode of κ-point photons of A_{1g} symmetry at 1357 cm^{-1} and the G-band arising due to the E_{2g} symmetry of sp^2 carbon at 1587 cm^{-1} confirms the formation of GO.[33,34] The D- and G-bands in AuNPs-rGO nanocomposite were observed at 1353 and 1594 cm^{-1}. The I_D/I_G ratios for GO and AuNPs-rGO were found to be 0.88 and 0.92 respectively. The higher value of this ratio for AuNPs-rGO suggests that overall defects in AuNPs-rGO have increased. This could be attributed to the fact that even though there is partial reformation of C=C network in AuNPs-rGO, the disruptions of sp^2 domains due to loss of carbon as CO_2 and interaction of gold with GO induces more defects in the GO structure.[24,26] Also the 2D band in AuNPs-rGO at 2940 cm^{-1} has a greater intensity than that of GO, pointing towards layered structure.[26,34,35] Furthermore, the structural integrity of the materials in their film forms was confirmed using FTIR and UV-visible spectroscopy (see details in the supporting information and **Figure S1**).

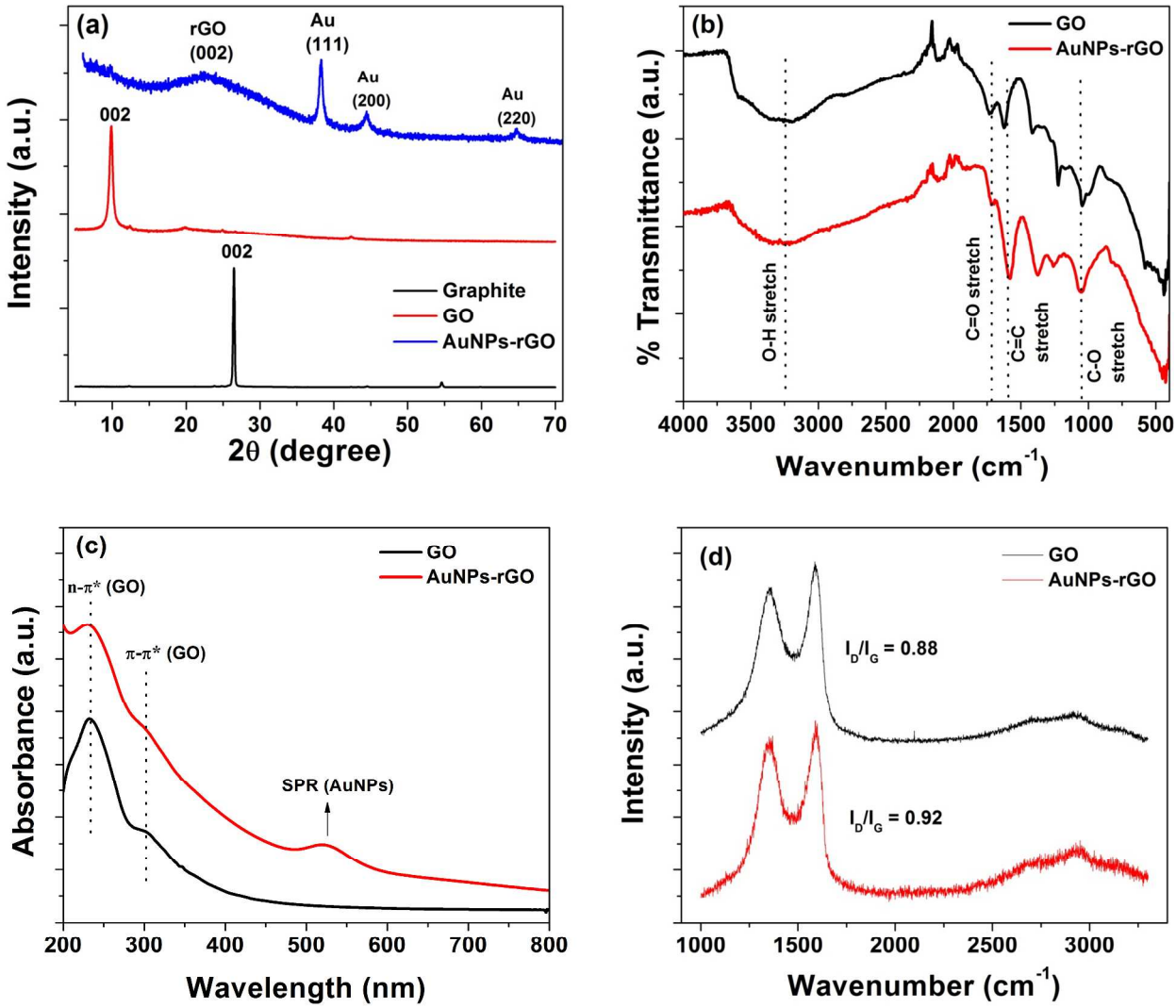

Figure 1. (a) Powder X-Ray diffraction spectra of graphite, GO and AuNPs-rGO samples. (b) FTIR spectra of as synthesized GO and AuNPs-rGO nanocomposite. (c) UV-Visible spectra of GO and AuNPs-rGO dispersion in water. (d) Raman spectra of GO and AuNPs-rGO powder samples.

The morphology of GO sheets and AuNPs-rGO is viewed by HR-TEM as shown in **Figure 2**. The TEM micrograph for GO reveals the formation of single or few layered two-dimensional sheets as evident by wrinkles and folds in the micrograph. On the other hand, TEM images of AuNPs-rGO composite shows monodispersed spherical Au nanoparticles uniformly distributed

on rGO sheets with very little aggregation. The average size of the nanoparticles is in the range of 16-18 nm with lattice spacing similar to what was obtained using XRD for AuNPs. Furthermore, to fabricate high performance electrodes, the loading and size of AuNPs on rGO sheets was optimized by varying the precursor compositions and verified using TEM measurements for other compositions (**Figure S4a and S5a** in supporting information).

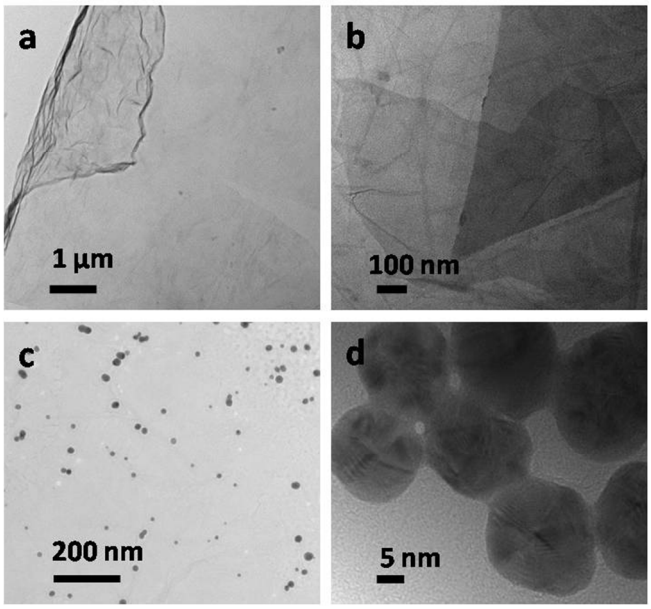

Figure 2. HR-TEM images of GO sheets (a and b) and AuNPs-rGO composite (c and d) at different scales.

The covalent immobilization of anti-IL8 on AuNPs-rGO/ITO electrode was corroborated by FTIR, AFM, XPS and electrochemical techniques. The FTIR spectra and AFM of AuNPs-rGO/ITO before and after anti-IL8 immobilization are shown in **Figure S2** of supporting information. XPS survey spectra exhibiting the characteristic features for GO, AuNPs-rGO and Anti-IL8/AuNPs-rGO films (on Si wafer) over a wide binding energy (BE) range have been shown in the supporting information (**Figure S3**). As expected, only the carbon and oxygen related features are seen in GO sample, along with substrate-related Si peaks, Au 4f-related

features are seen for AuNPs-rGO sample. The appearance of Na signal for AuNPs-rGO is attributed to the adsorption of Na^+ from trisodium citrate that was used to reduce Au^{3+} to Au nanoparticles. The tiny feature of Au 4f is shown by the zoomed region within inset for clarity. For Anti-IL8/AuNPs-rGO, a N 1s peak appears along with all other features seen for AuNPs-rGO due to the presence of amide bonds in the protein. We also acquired high resolution spectra of Au 4f core levels for AuNPs, AuNPs-rGO and Anti-IL8/AuNPs-rGO as shown in **Figure 3a**. For AuNPs, spin orbit splitted components Au $4f^{7/2}$ and Au $4f^{5/2}$ appear at 83.95 and 87.6 eV, respectively and it confirms that AuNPs are in Au^0 valence state.[35,36] No significant change in the BE position of Au 4f peaks between pure AuNPs, AuNPs-rGO and Anti-IL8/AuNPs-rGO was observed, indicating that the AuNPs are loosely bonded to the rGO surface in AuNPs-rGO and Anti-IL8/AuNPs-rGO. This suggested that no charge transfer takes place between AuNPs and rGO as well as between AuNPs and IL8 antibodies. **Figure 3b** contains the C 1s core levels for GO, AuNPs-rGO and Anti-IL8/AuNPs-rGO along with fitting components. Five gaussian peaks were used for each C 1s core level to achieve satisfactory fitting of the data. The main peak is related to sp^2 bonded carbon atoms (C=C) and it appears at 284.5 eV BE for GO and other components can be assigned to C–OH (285.9 eV), C-O (286.8 eV), C=O (287.5 eV) and –COOH (288.4 eV),[37-39] corroborating the FTIR results. For AuNPs-rGO, a significant reduction in the C-O component is clearly seen when compared to GO (**Table 1**) and relative increase in the abundance of C=C in the AuNPs-rGO which is again in agreement with FTIR data. Even though relative contribution of other functional groups remain almost similar, interestingly we see clear increase in intensity around the BE region assigned to C-OH component for Anti-IL8/AuNPs-rGO (**Table 1**). This BE position is very close to what is expected for C-N bonds and we can ascribe this extra intensity as evidence of attachment of anti-IL8 antibodies to the AuNPs-rGO

composite. We see a clear N 1s signal from Anti-IL8/AuNPs-rGO sample (**Figure 3c**). The BE position of N 1s is found to be at 399.65 eV close to the BE value for amide (NH-C=O).[40,41] This ~~is~~ shows direct evidence of the attachment of the anti-IL8 antibodies to the AuNPs-rGO composite.

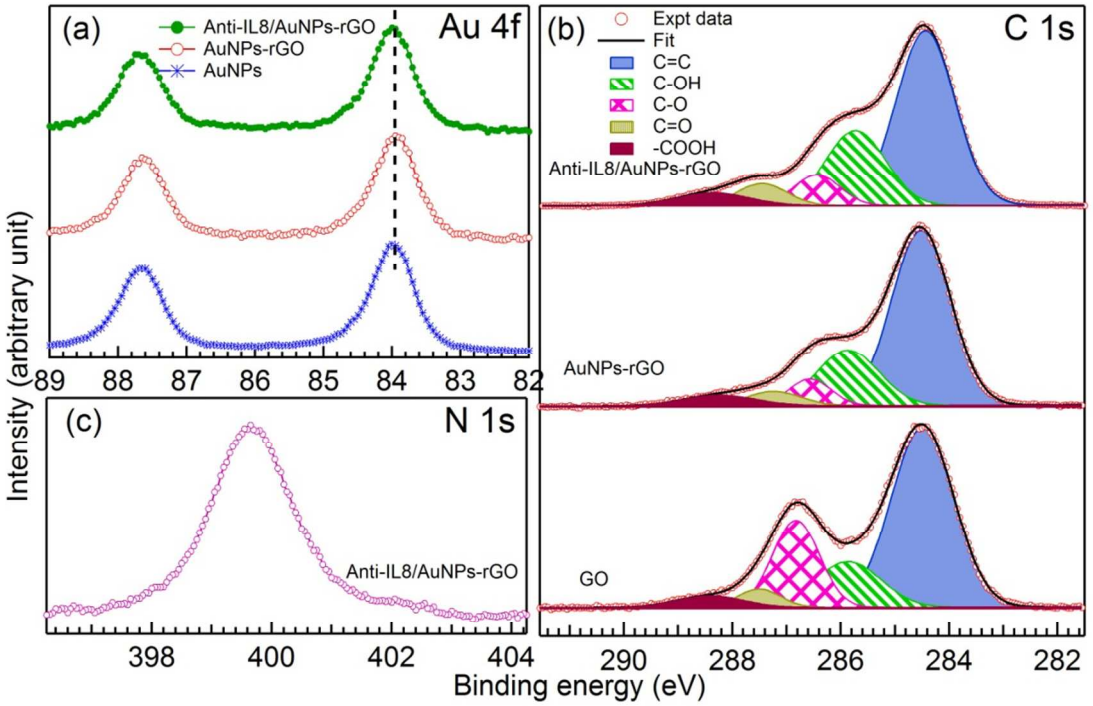

Figure 3: XPS studies (a) Au 4f core levels for pure AuNPs, AuNPs-rGO and Anti-IL8/AuNPs-rGO samples. Dashed line indicates peak positions. All the spectra have been normalized to have same peak height at the highest peak for convenience of comparison. Spectra have been staggered vertically for clarity of presentation; (b) C 1s core level spectra (open circles) for GO, AuNPs-rGO and Anti-IL8/AuNPs-rGO samples. Fitted data (solid line) and deconvoluted fitting components (shaded and patterned regions) are also shown here. (c) N 1s core level spectrum from Anti-IL8/AuNPs-rGO sample.

Table 1. Summary of fitting parameters for the C 1s core-level spectra (Fig. 2(b)) for GO, AuNPs-rGO, and Anti-IL8/AuNPs-rGO samples. Uncertainty in determining the BE position and

full width at half maximum (FWHM) is estimated to be ±0.05 eV. Uncertainty in determining relative percentage is estimated to be ±5% of the base value.

GO				**AuNPs-rGO**			**Anti-IL8/AuNPs-rGO**		
Peak	**BE (eV)**	**FWHM (eV)**	**Relative %**	**BE (eV)**	**FWHM (eV)**	**Relative %**	**BE (eV)**	**FWHM (eV)**	**Relative %**
C=C	284.5	1.35	56.8	284.5	1.3	62.8	284.4	1.3	56.4
C-OH	285.9	1.4	14.9	285.9	1.35	20.9	285.7	1.3	24.6
C-O	286.8	1.0	20.3	286.6	0.9	6.8	286.4	1.0	7.6
C=O	287.5	0.9	4.0	287.2	1.1	4.7	287.4	1.2	6.2
-COOH	288.4	1.5	4.0	288.2	1.6	4.8	288.3	1.6	5.2

The electron transfer mechanism of the $[Fe(CN)_6]^{3-/4-}$ redox process at GO/ITO and optimized AuNPs-rGO/ITO electrodes (**Figure S4b, S4c and S5b** in supporting information) was studied comprehensively using CV. The CV of both the electrodes were recorded at different scan rates ($0.01 – 0.15\ Vs^{-1}$) in 3 mM Zobell's solution showing an increase in redox peak current (I_p) with increasing scan rate in both cases (**Figures 4a and 4b**). The forward-to-backward peak current ratios (I_{pa}/I_{pc}) in the range of 1.06 – 1.10 indicate the quasi-reversibility of both systems.[42] The insets in **Figures 4a and 4b** show the plot of anodic and cathodic peak currents vs square root of scan rate for GO/ITO and AuNPs-rGO/ITO systems, respectively. The linear variations of peak current with square root of scan rate for AuNPs-rGO/ITO electrode with regression coefficient (R^2) values of 0.99945 and 0.99921 for I_{pa} and I_{pc} respectively, indicate diffusion controlled processes at the electrode. The GO/ITO electrode also exhibited almost linear variation in peak

current *vs* square root of scan rate but the broader redox peaks indicate slow diffusion controlled processes compared to AuNPs-rGO/ITO electrode.

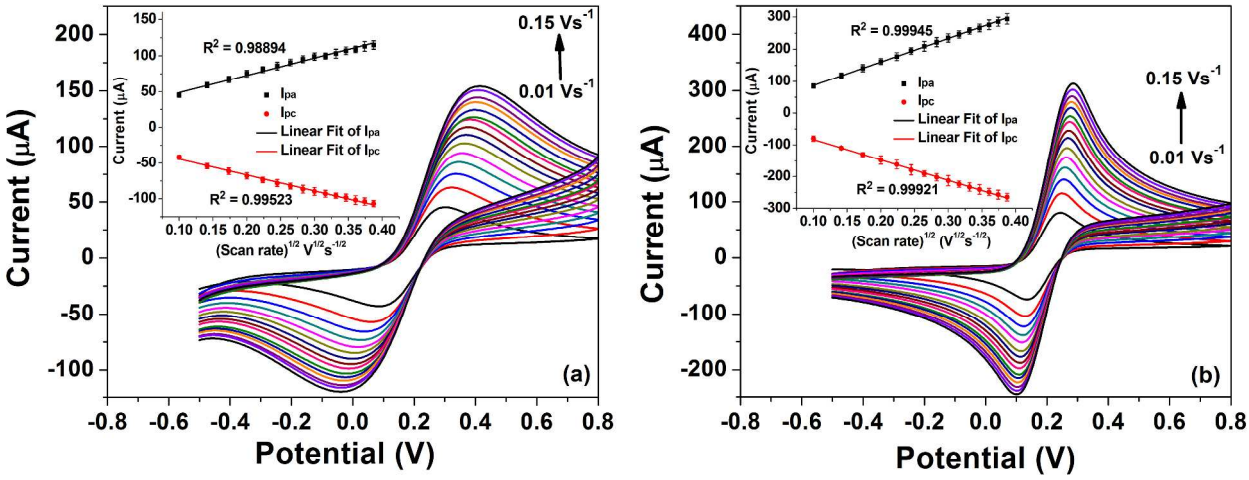

Figure 4. Cyclic Voltammetry curves of 3 mM Zobell's solution measured at different scan rates (0.01 – 0.15 Vs^{-1}) at (a) GO/ITO and (b) AuNPs-rGO/ITO electrodes. Inset: Plots of peak currents vs square root of scan rates for (a) GO/ITO and (b) AuNPs-rGO/ITO electrodes.

Further, the diffusion coefficients of the redox processes at the two electrodes were calculated using Randles-Sevcik equation.[42,43]

$$I_p = (2.69 \times 10^5) n^{3/2} A C D^{1/2} v^{1/2} \qquad (1)$$

where, I_p is the peak current in amperes, n is the number of electrons transferred in the oxidation/reduction process (here n = 1), A is the area of electrode in cm^2 (active surface area, A, in our case is 0.25 cm^2), C is the concentration of electroactive species in mol/cm^3 (here it is 3×10^{-6} mol/cm^3 of Zobell's solution), D is the diffusion coefficient in cm^2/s and v is the scan rate in Vs^{-1}. Using this equation, the diffusion coefficient for GO/ITO was found to be 1.2107×10^{-6} $cm^2\ s^{-1}$ whereas, for AuNPs-rGO/ITO it was 1.0816×10^{-5} $cm^2\ s^{-1}$. The higher diffusion

coefficient for AuNPs-rGO/ITO indicates better electron transfer rate compared to GO/ITO matrix which is a crucial parameter in defining the sensitivity of a biosensing electrode.

The variation of anodic and cathodic peak potential separation (ΔE_p) with scan rate tells the reversible or irreversible nature of any electrochemical process. For reversible processes, ΔE_p remains constant at all scan rates, but it starts increasing as the system goes towards irreversibility. The greater ΔE_p values along with broadness of redox peaks for GO/ITO signifies slower diffusion rate where mass transfer dominates the charge transfer process at electrode surface.[44] The standard heterogeneous electron-transfer rate constant, k°, for two electrode systems were evaluated using Nicholson's method,[45] using the following equation:

$$\Psi = k^{o} [\pi D n \nu F/RT]^{-1/2} \quad (2)$$

where Ψ is the Nicholson's kinetic parameter as a function of ΔE_p, while the other symbols are same as in equation 1. Values of Ψ were determined using the following empirical equations given by Lavagnini et al.[46] and were plotted against $[\pi D n \nu F/RT]^{-1/2}$ (see **Figure S6** in supporting information).

$$\Psi = \left(-0.6288 + 0.0021\, n\, \Delta E_p\right)/(1 - 0.017\, n\, \Delta E_p) \quad \text{for } \Delta E_p < 200 \text{ mV} \quad (3)$$

$$\Psi = 2.18\, [\beta/\pi]^{1/2} \exp[-(\beta^2 F/RT) n\, \Delta E_p] \quad \text{for } \Delta E_p > 200 \text{ mV (where } \beta = 0.5) \quad (4)$$

The slope obtained from the linear fitting of this curve gave the heterogeneous rate constant k° which was found to be 1.14×10^{-3} cm s^{-1} for GO/ITO and 2.19×10^{-3} cm s^{-1} for AuNPs-rGO/ITO.

Further, the electron transfer kinetics for AuNPs-rGO/ITO electrode along with GO/ITO, rGO/ITO and AuNPs/ITO electrodes were studied using EIS by monitoring the change in real

part of electrode impedance on Nyquist plot.[42,47] The charge transfer resistance (R_{CT}) values were found to be 730.78, 400.69, 252.75 and 152.20 Ω for GO/ITO, rGO/ITO, AuNPs/ITO and AuNPs-rGO/ITO electrodes, respectively, as shown in **Figure 5a**. The lower R_{CT} value for AuNPs-rGO/ITO compared to other electrodes reveals the rapid electron transfer kinetics at the electrode/electrolyte interface, corroborating the results obtained from cyclic voltammetry (**Figure 5b**) and suggesting the suitability of the AuNPs-rGO/ITO matrix for immunosensor fabrication.

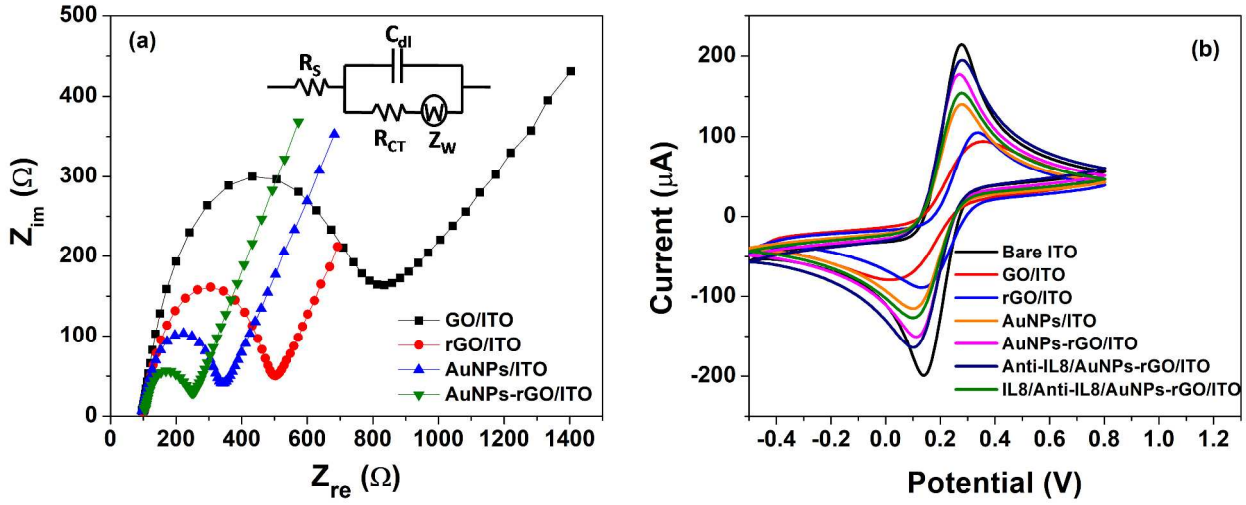

Figure 5. (a) Nyquist plot for GO/ITO, rGO/ITO, AuNPs/ITO and AuNPs-rGO/ITO obtained in 3 mM Zobell's solution at potential of 0.2 V in the frequency range of 0.1 Hz to 100 kHz. (b) Cyclic voltammetry curves at 0.05 Vs^{-1} scan rate in 3 mM Zobell's solution at various fabricated electrodes.

The enhanced electron transfer kinetics for the AuNPs-rGO/ITO electrode is attributed to the presence of AuNPs on rGO which act as small conduction pockets for the diffusion of charge from solution to the electrode surface.[48] Furthermore, the enhanced π-conjugated network of rGO in the composite as compared to GO, helps in channeling the electron flow more efficiently.

Henceforth, the AuNPs-rGO/ITO electrode is modified with anti-IL8 antibodies for the fabrication of the immunosensor. The stepwise surface modifications of ITO (i.e. GO/ITO, rGO/ITO, AuNPs/ITO, AuNPs-rGO/ITO, Anti-IL8/AuNPs-rGO/ITO and IL8/Anti-IL8/AuNPs-rGO/ITO) electrode were characterized by recording CV in 3 mM Zobell's solution at the scan rate of 0.05 Vs^{-1} as shown in **Figure 5b**. The higher redox current for AuNPs-rGO/ITO electrode compared to AuNPs/ITO, rGO/ITO and GO/ITO electrodes indicates the synergistic role of rGO and AuNPs in electron transfer process in AuNPs-rGO composite. The increase in redox peak current for Anti-IL8/AuNPs-rGO/ITO electrode compared to bare AuNPs-rGO/ITO electrode is attributed to the presence of protonated amine groups[49] on anti-IL8 (at pH 7.4) which facilitate the diffusion of negatively charged $[Fe(CN)6]^{3-/4-}$ on to the electrode surface through electrostatic interactions. Consequently, the high adsorption of these species on the electrode surface, contributes to an increase in the redox peak current.[50] The increase in redox current indicates successful immobilization of antibody molecules. On the other hand, a significant decrease in redox peak current was observed upon binding of the IL8 analyte to the Anti-IL8/AuNPs-rGO/ITO immunoelectrode. The decrease in current is ascribed to the antigen-antibody binding through noncovalent interactions (i.e., van der Waals, hydrophobic, electrostatic, hydrogen-bonding etc.), and the formation of a slightly non-conductive layer on the electrode surface that restricts electron mobility.[51] The variation in values of I_{pa}, I_{pc} , ΔE_p and surface concentration (γ) of electro-active species at electrode surface (which is calculated using Brown-Anson model[52]) after each surface modification step, are shown in **Table 2**.

Table 2. Variation in I_{pa}, I_{pc}, ΔE_p and γ after each surface modification step of the electrode.

Electrode	I_{pa} **(μA)**	I_{pc} **(μA)**	ΔE_p **(V)**	γ **(mol cm^{-2})** $I_{pa} = \frac{n^2F^2\gamma Av}{4RT}$
Bare ITO	217	-211	0.131	1.848×10^{-8}
GO/ITO	80	-73	0.309	6.813×10^{-9}
rGO/ITO	105	-89	0.205	8.942×10^{-9}
AuNPs/ITO	140	-117	0.180	1.192×10^{-8}
AuNPs-rGO/ITO	157	-144	0.147	1.337×10^{-8}
Anti-IL8/AuNPs-rGO/ITO	193	-172	0.167	1.643×10^{-8}
IL8/Anti-IL8/AuNPs-rGO/ITO	153	-133	0.167	1.303×10^{-8}

The antibody concentration to be immobilized on electrode surface, immuno-reaction time and pH were optimized for the fabrication of the immunosensor. The maximum concentration used for immobilization was optimized by measuring the analytical signal for antibodies in the concentration range of 100 ng mL^{-1} to 5μg mL^{-1}. It has been observed that the current increases with increase in antibody concentration, attaining the highest value at 1μg mL^{-1}, after which it decreases slightly and becomes almost constant (**Figure 6a**), due to full occupancy of the active sites. Therefore, 1μg mL^{-1} antibody concentration was selected for immobilization onto the AuNPs-rGO/ITO electrode for the fabrication of immunosensor. The minimum incubation time required for effective analyte interaction was determined by varying the duration of incubation time of antibody-antigen interaction from 3 to 18 min. **Figure 6b** shows that the response current decreases initially, reaching the lowest current limit at 9 min after which no significant change is observed in the analytical signal. Hence, the response time of the immunoelectrode for analyte detection is selected to be 9 min. The effect of pH values on the immunoreaction was determined by measuring the current signal at different pH ranging from 5.8 to 8.0 (**Figure 6c**). The current

decreases from 5.8 to higher pH values, stabilizing after pH 7.2. Based on these observations an intermediate value of pH 7.4 was used for subsequent experiments.

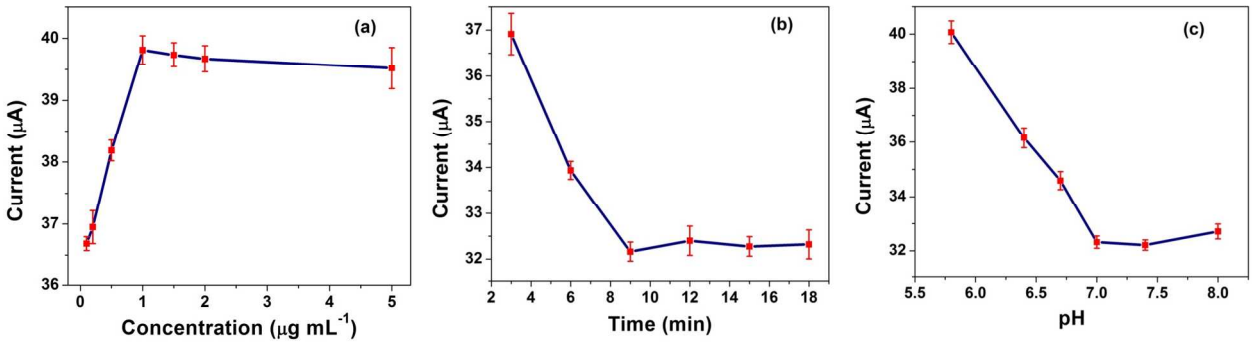

Figure 6. Experiments for the optimization of (a) concentration of anti-IL8 for immobilization (b) antigen i.e. IL8 incubation time and (c) working buffer (10 mM PBS) pH on the immunoreaction.

In contrast to the standard CV technique, DPV is a highly sensitive technique as it gives peak corresponding to only faradaic current, and was therefore used to measure the response studies of the fabricated immunoelectrode. **Figure 7a** shows the analytical performance of the Anti-IL8/AuNPs-rGO/ITO immunoelectrode using DPV for different concentrations of the IL8 antigen ranging from 500 fg/mL to 50 ng/mL. The DPV scans reveal the binding of antigen in the form of a decrease in response current with increasing antigen concentration. The decrease in current is attributed to hindered electron transfer due to the formation of an insulating layer as a result of increased antigen binding. The fabricated immunosensor exhibits a linear response in the analyte concentration range of 500 fg mL^{-1} - 4 ng mL^{-1} as shown in **Figure 7b**. The linear regression coefficient is calculated using following equation.

$$I_p = -0.00731\,[\text{IL8 conc.}] + 39.24457,\ R^2 = 0.99758 \quad (5)$$

Further, the limit of detection (*LOD*) of the Anti-IL8/AuNPs-rGO/ITO immunosensor was determined using the following equation.[21]

$$LOD = k \times \sigma/S \quad (6)$$

Where k is the confidence level parameter (k = 3 with statistical confidence of 99.6%), σ is the standard deviation of blank measurements (RSD for 5 measurements is taken here) and S is the sensitivity of the electrode which is equal to the slope ($\Delta I/\Delta C$) of current vs concentration plot. Taking into account all the above parameters, the *LOD* of the fabricated electrode was calculated as 72.73±0.18 pg mL^{-1}.

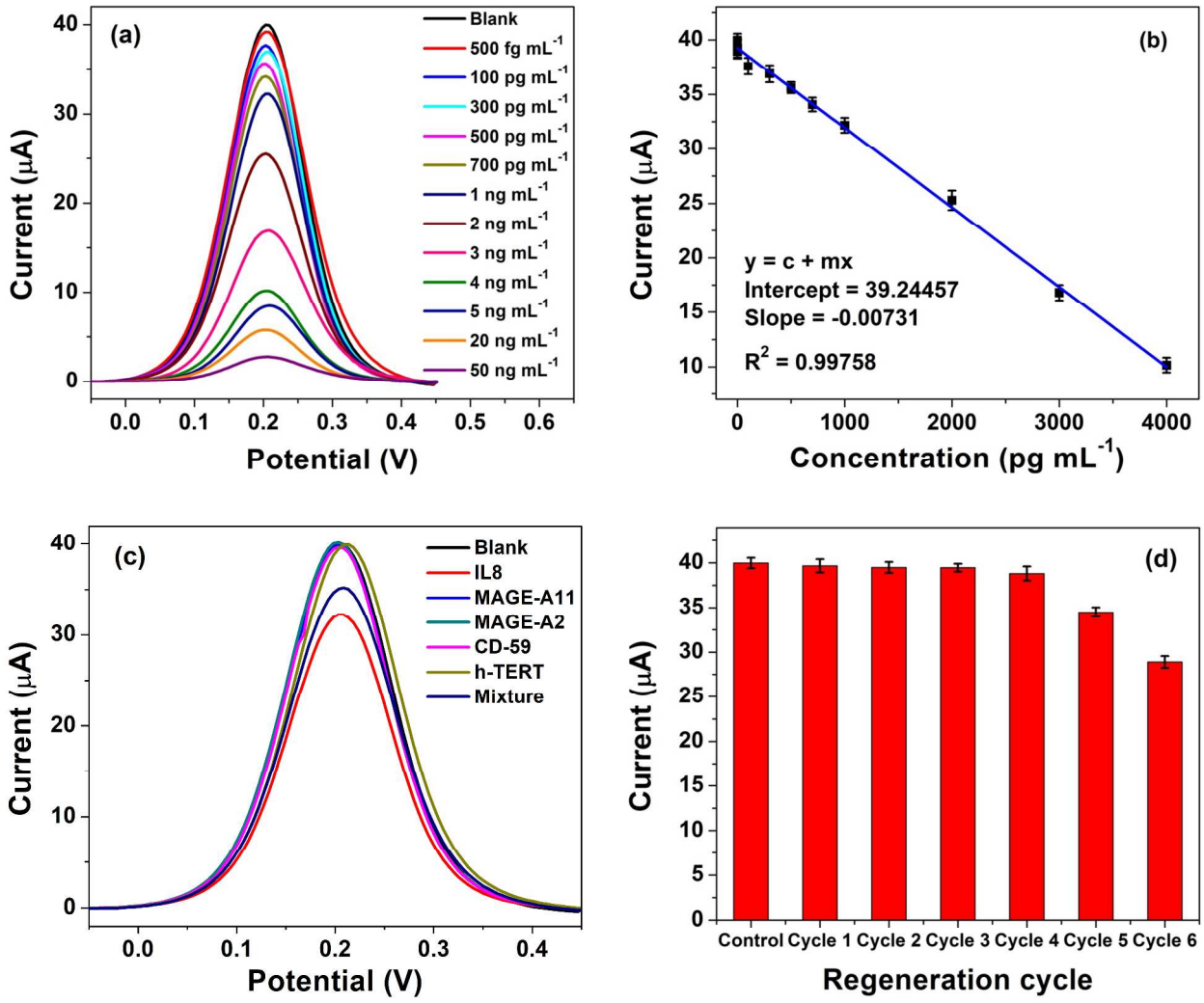

Figure 7. (a) DPV curves showing response studies of the immunosensor towards different concentrations (500 fg mL^{-1} - 50 ng mL^{-1}) of IL8. (b) Calibration curve of IL8 in the linearity range of 500 fg mL^{-1} - 4 ng mL^{-1}. (c) DPV curves showing specificity of the immunosensor and (d) Bar graph showing regeneration of the immunoelectrode.

The selectivity of the fabricated oral cancer immunosensor was investigated by exposing it to other cancer biomarkers like MAGE-A11, MAGE-A2, CD59 and hTERT. A 1 ng mL^{-1} concentration of each of these interferants was used for binding with Anti-IL8/AuNPs-rGO/ITO and their detection was measured using DPV. The immunosensor showed exceptionally high specificity for IL8 compared to the other biomarkers. Furthermore, a mixture of above mentioned biomarkers along with IL8 was allowed to bind with Anti-IL8/AuNPs-rGO/ITO immunoelectrode. The immunoelectrode exhibited the analytical signal corresponding to IL8 only, as shown in **Figure 7c**. The other antigens showed negligible change in current compared to blank (i.e. Anti-IL8/AuNPs-rGO/ITO) indicating that there is no interaction between the antibody and non-specific antigen molecules.

The immunosensor was further analyzed for its reproducibility by using a set of five immunoelectrodes for detecting IL8 (1 ng mL^{-1}). The RSD of 2.7 % in the analytical signal from all the five immunoelectrodes indicate the reproducible fabrication of the immunosensor. Regeneration of the immunosensor could be assessed by subjecting the antigen bound immunoelectrodes to either highly acidic or highly basic pH to release the antigen. In our case the immunoelectrode was dipped for 80 s in 30 mM NaOH solution (pH = 12.4) followed by washing with 10 mM PBS and tested using DPV. **Figure 7d** shows six subsequent regeneration cycles of the immunoelectrode recorded in triplicate. The immunosensor showed a maximum deflection of 1.4 % after 3 regeneration cycles and an increase to 2.9 % after 4th regeneration

cycle. After the 5th regeneration cycle however, it retained only 86.3 % of the signal which further decreased to 72.3 % after 6th cycle suggesting that the immunosensor could be reused efficiently for four times.

Furthermore, the biochemical activity of the immunosensor was examined over a period of time to determine its stability. The sensor was stored at 4 ºC and its DPV was measured every week by treating it with 700 pg mL^{-1} IL8. The sensor retained 97.9 % activity after one month, 95.6 % activity after two months and 94.3 % of activity after the end of third month, after which the activity dropped to 91.8 % in the fourth month, and then declined significantly afterwards. Hence, it could be concluded that the biosensor works reliably for up to three months.

To investigate the performance of the fabricated immunosensor in real biological samples, saliva of healthy human was spiked with five different concentrations (500, 700, 1000, 2000 and 3000 pg mL^{-1}) of IL8 and detected using DPV (**Figure 8a**). The incubation time (9 min) for antibody-antigen interaction was the same as in previous experiment. A similar trend ~~of~~ showing a decrease in response current signal with increasing concentration was observed for the spiked saliva samples. The response signals for the five concentrations fit in the following linear regression equation:

$$I_p = -0.00698\,[\text{IL8 conc.}] + 37.76711,\ R^2 = 0.98758 \qquad (7)$$

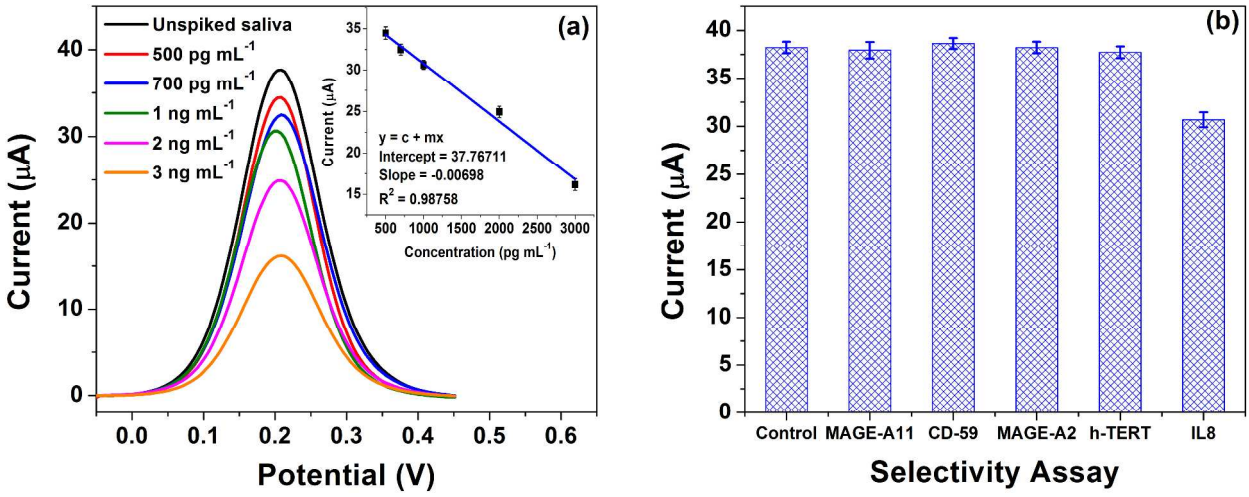

Figure 8. (a) DPV curves showing response of the immunoelectrode towards different concentrations of spiked saliva samples. Inset: Calibration curve of the saliva samples. (b) Bar graph for selectivity of the immunoelectrode in salivary environment.

The % recovery values of IL8 in the saliva samples were evaluated using equation 8 and are shown in **Table 3**.

$$\%\ Recovery = \frac{x_i - x_o}{x_s} \times 100 \qquad (8)$$

where x_i and x_o respectively, are the estimated concentrations of analyte in spiked and unspiked samples as determined from the calibration plot of standard samples, respectively, and x_s is the actual concentration of spiked IL8. The oral cancer immunosensor exhibited an average recovery value of 94.15 % for IL8 in spiked saliva samples.

Table 3. Estimation of IL8 in spiked saliva samples.

Actual Conc. (x_s) **(pg mL^{-1})**	**Estimated conc.** (x_i) **(pg mL^{-1})**	**Calculated conc.** $(x_i - x_o)$ **(pg mL^{-1})** x_o**= 214.65 pg mL^{-1}**	**Recovery (%)**

500	653.67	439.02	87.80
700	925.26	710.61	101.51
1000	1177.56	962.91	96.29
2000	1957.70	1743.05	87.15
3000	3156.00	2941.35	98.04

The specificity of the immunosensor was explored in saliva as well by using saliva samples spiked with the other non-specific biomarkers (MAGE-A11, CD-59, MAGE-A2, h-TERT) and testing using DPV (**Figure 8b**). The results obtained were in close agreement with that of the standard samples. Only IL8 sample showed a decrease in peak current, while the other antigens showed peaks similar to the control. Anti-IL8/AuNPs-rGO/ITO immunoelectrodes could sense very low levels of IL8 in saliva showing their potential for oral cancer detection. A comparison of the already developed oral cancer biosensors with the present work is shown in **Table 4**.

Table 4. List of the matrix systems and response techniques used in earlier reported oral cancer biosensors.

S. No.	Matrix	Label	Analyte	Detection range	Limit of Detection	Time	Technique	Reference
1.	Anti-IL8 IgG1 (MAB208)/CM5 Sensor chip		IL8	9.5-191 pM	2.5 pM (in buffer) 184 pM (in saliva)	13 min	Surface Plasmon Resonance	53
2.	IL8 specific capture probe/ Streptavidin coated coverslips	Flourescent probes	IL8	6 fM-12 pM	4 fM (in buffer)	30 min	Optical Microscope	54

3.	Anti-IL6/SWNTs/Graphite	Horseradish Peroxidase (HRP)	IL6	0.5-30 pg mL^{-1}	0.5 pg mL^{-1} (in calf serum)	60 min	Amperometry	55
4.	Gold/MCH/Signalling probe T1electrode	Label-free	DNA (Oral cancer overexpressed 1)	0.08-8.0 fM	0.02 fM (for complementary target DNA)	60 min	Amperometry	56
5.	Anti-IL8/GSH-AuNP/Pyrolytic graphite	Superpara magnetic beads with HRP	IL8	1-500 fg mL^{-1}	1 fg mL^{-1} (in serum)	--	Amperometry	57
6.	Capture probe-modified magnetic beads/magnetically controllable gold electrode	streptavidin-HRP	RNA	1 aM-10 fM	0.22 aM (for complementary target miRNA)	120 min	Amperometry	58
7.	ITO combined with nicking endonuclease signal amplification (NESA)	Label-free	DNA (Oral cancer overexpressed 1)	1-10 pM	0.35 pM (for target DNA)	90 min	Differential Pulse Voltammetry	59
8.	Anti-CYFRA-21–1/APTES/ ZrO_2/ITO	Label-free	CYFRA-21-1	2-16 ng mL^{-1}	0.08 ng mL^{-1} (in buffer)	20 min	Cyclic Voltammetry	50
9.	Anti-CD59/Cystein/Au	Label-free	CD59	1-1000 fg mL^{-1}	0.84 fg mL^{-1} (in spiked saliva)	10 min	Electrochemical Impedance Spectroscopy	60
10.	Magnetic beads/Screen printed electrodes	HRP	IL8	--	72.4 pg mL^{-1} (in saliva)	--	Amperometry	61
11.	Anti-IL8/AuNPs-rGO/ITO	Label-free	IL8	500 fg mL^{-1} -50 ng mL^{-1}	72.73 pg mL^{-1} (in buffer)	9 min	Differential Pulse Voltammetry	Our Study

4. CONCLUSION

A highly selective, label-free and non-invasive immunosensing platform based on AuNPs-rGO nanocomposite thin films, for early level detection of salivary oral cancer biomarker IL8 has been developed. The synergy in electronic and electrochemical properties of rGO and AuNPs in the AuNPs-rGO composite enhances the electron transfer rate, which in turn leads to the fast and efficient detection of IL8 with a response time of only 9 min. The *LOD* of 72.73±0.18 pg mL^{-1} exhibited by the immunosensor is well below the clinical salivary expression level of IL8 (720 pg mL^{-1}) in an average oral cancer patient. The immunosensor showed excellent performance in saliva with a 94.15 % average recovery of IL8 in spiked saliva. The high specificity, precision and stability exhibited by the fabricated immunosensor makes it a promising platform for early stage oral cancer detection, which can be easily modified for detecting other cancer types, and only requires samples from body fluids such as saliva, blood and urine for detection of cancer-specific biomarkers.

ASSOCIATED CONTENT

Supporting Information. FTIR and UV-Vis spectra of GO/ITO and AuNPs-rGO/ITO electrodes (Figure S1). FTIR spectra and AFM images of AuNPs-rGO film before and after immobilization (Figure S2). XPS survey spectra for GO, AuNPs-rGO and IL8-AuNPs-rGO samples (Figure S3). Optimization of AuNPs-rGO composite electrode in terms of AuNPs size and loading density onto rGO (Figure S4 and S5). Plot of Nicholson's kinetic parameter (Ψ) vs $[\pi Dn\nu F/RT]^{-1/2}$ for GO/ITO and AuNPs-rGO/ITO electrodes (Figure S6). DPV and

regeneration graphs showing optimization of antibody immobilization method (Figure S7).

AUTHOR INFORMATION

Corresponding Author

*Email: singh.uprm@gmail.com

*Email: pritichem@gmail.com

Author Contributions

The manuscript was written through contributions of all authors. All authors have given approval to the final version of the manuscript.

ACKNOWLEDGMENT

Director, CSIR-National Physical Laboratory, New Delhi is gratefully acknowledged for his keen interest in the work and encouragements. We thank Dr. Praveen Saini for providing access to his research facilities. PS and SV sincerely acknowledge support from DST Inspire Faculty project (IFA12-CH-31), SPS acknowledges the support from CSIR-Network project BSC0112. KA duly acknowledges funding from UPoE-II (158,161), JNU and AS acknowledges the funding from UGC (F.15-1/2016-17/PDFWM-2015-17-UTT-33566(SA-II)).

ABBREVIATIONS

AuNPs-rGO, Gold nanoparticles-reduced graphene oxide; IL8, Interleukin 8; EDC, N-Ethyl-N′-(3-dimethylaminopropyl) carbodiimide hydrochloride; NHS, N-Hydroxysuccinimide; ITO, Indium tin oxide.

REFERENCES

(1) Neville, B. W.; Day, T. A. Oral Cancer and Precancerous Lesions. *CA Cancer J Clin.* **2002**, *52*, 195-215.

(2) Massano, J.; Regateiro, F. S.; Januário, G.; Ferreira, A. Oral Squamous Cell Carcinoma: Review of Prognostic and Predictive Factors. *Oral Surg. Oral Med. Oral Pathol. Oral Radiol. Endod.* **2006**, *102*, 67-76.

(3) Warnakulasuriya, S. Global Epidemiology of Oral and Oropharyngeal Cancer. *Oral Oncol.* **2009**, *45*, 309–316.

(4) Brocklehurst, P.; Kujan, O.; O'Malley, L. A.; Ogden, G.; Shepherd, S.; Glenny, A. M. Screening Programmes for the Early Detection and Prevention of Oral Cancer. *Cochrane Database Syst. Rev.* **2013**, *11*, CD004150.

(5) Gupta, B.; Ariyawardana, A.; Johnson, N. W. Oral Cancer in India Continues in Epidemic Proportions: Evidence Base and Policy Initiatives. *Int. Dent. J.* **2013**, *63*, 12–25.

(6) Siegal, R. L.; Miller, K. D.; Jemal, A. Cancer Statistics, 2017. *CA Cancer J Clin.* **2017**, *67*, 7-30.

(7) Lisa Cheng, Y.-S.; Wright, J. Advances in Diagnostic Adjuncts for Oral Squamous Cell Carcinoma. *Open Pathol. J.* **2011**, *5*, 3-7.

(8) Mehrotra, R.; Gupta, D. K. Exciting New Advances in Oral Cancer Diagnosis: Avenues to Early Detection. *Head Neck Oncol.* **2011**, *3*, 33.

(9) Wu, L.; Qu, X. Cancer Biomarker Detection: Recent Achievements and Challenges. *Chem. Soc. Rev.* **2015**, *44*, 2963-2997.

(10) Kelloff, G. J.; Sigman, C. C. Cancer Biomarkers: Selecting the Right Drug for the Right Patient. *Nat. Rev. Drug Discovery* **2012**, *11*, 201-214.

(11) Watanabe, H.; Iwase, M.; Ohashi, M.; Nagumo, M. Role of Interleukin-8 Secreted from Human Oral Squamous Cell Carcinoma Cell Lines. *Oral Oncol.* **2002**, *38*, 670–679.

(12) Xie, K. Interleukin-8 and Human Cancer Biology. *Cytokine Growth Factor Rev.* **2001**, *12*, 375–391.

(13) St. John, M. A.; Li, Y.; Zhou, X.; Denny, P.; Ho, C. M.; Montemagno, C. D.; Shi, W.; Qi, F.; Wu, B.; Shinha, U.; Jordan, R.; Wolinsky, L.; Park, N. H.; Liu, H.; Abemayor, E.; Wong, D. T. W. Interleukin 6 and Interleukin 8 as Potential Biomarkers for Oral Cavity and Oropharyngeal Squamous Cell Carcinoma. *Arch. Otolaryngol. Head Neck Surg.* **2004**, *130*, 929–935.

(14) Rusling, J. F.; Kumar, C. V.; Gutkinde, J. S.; Patel, V. Measurement of Biomarker Proteins for Point-of-Care Early Detection and Monitoring of Cancer. *Analyst* **2010**, *135*, 2496–2511.

(15) Nimse, S. B.; Sonawane, M. D.; Song, K.-S.; Kim, T. Biomarker Detection Technologies and Future Directions. *Analyst* **2016**, *141*, 740-755.

(16) Ronkainen, N. J.; Halsallb, H. B.; Heineman, W. R. Electrochemical Biosensors. *Chem. Soc. Rev.* **2010**, *39*, 1747–1763.

(17) Chikkaveeraiah, B. V.; Bhirde, A. A.; Morgan, N. Y.; Eden, H. S.; Chen, X. Electrochemical Immunosensors for Detection of Cancer Protein Biomarkers. *ACS Nano* **2012**, *6*, 6546–6561.

(18) Rusling, J. F.; Sotzing, G.; Papadimitrakopoulos, F. Designing Nanomaterials-Enhanced Electrochemical Immunosensors for Cancer Biomarker Proteins. *Bioelectrochemistry* **2009**, *76*, 189-194.

(19) Kerman, K.; Saito, M.; Yamamura, S.; Takamura, Y.; Tamiya, E. Nanomaterial-Based Electrochemical Biosensors for Medical Applications. *Trends Anal. Chem.* **2008**, *27*, 585-592.

(20) Ronkainen N. J.; Okon, S. L.; Nanomaterial-Based Electrochemical Immunosensors for Clinically Significant Biomarkers. *Materials* **2014**, *7*, 4669-4709.

(21) Tiwari, J. N.; Vij, V.; Kemp, K. C.; Kim, K. S. Engineered Carbon-Nanomaterial-Based Electrochemical Sensors for Biomolecules. *ACS Nano* **2016**, *10*, 46−80.

(22) Gutés, A.; Hsia, B.; Sussman, A.; Mickelson, W.; Zettl, A.; Carraroa, C.; Maboudian, R. Graphene Decoration with Metal Nanoparticles: Towards Easy Integration for Sensing Applications. *Nanoscale* **2012**, *4*, 438-440.

(23) Cote, L. J.; Kim F.; Huang, J. Langmuir-Blodgett Assembly of Graphite Oxide Single Layers. *J. Am. Chem. Soc.* **2009**, *131*, 1043-1049.

(24) Song, J.; Xu, L.; Xing, R.; Li, Q.; Zhou, C.; Liu, D.; Song, H. Synthesis of Au/Graphene Oxide Composites for Selective and Sensitive Electrochemical Detection of Ascorbic Acid. *Sci. Rep.* **2014**, *4*, 7515.

(25) Moon, I. K.; Lee, J.; Ruoff, R. S.; Lee, H. Reduced Graphene Oxide by Chemical Graphitization. *Nat. Commun.* **2010**, *1*, 73.

(26) Zhang, Z.; Chen, H.; Xing, C.; Guo, M.; Xu, F.; Wang, X.; Gruber, H. J.; Zhang, B.; Tang, J. Sodium Citrate: A Universal Reducing Agent for Reduction / Decoration of Graphene Oxide with Au Nanoparticles. *Nano Res.* **2011**, *4*, 599-611.

(27) Marcano, D. C.; Kosynkin, D. V.; Berlin, J. M.; Sinitskii, A.; Sun, Z.; Slesarev, A.; Alemany, L. B.; Lu, W.; Tour, J. M. Improved Synthesis of Graphene Oxide. *ACS Nano* **2010**, *4*, 4806–4814.

(28) Zhang, N.; Qiu, H.; Liu, Y.; Wang, W.; Li, Y.; Wang, X.; Gao, J. Fabrication of Gold Nanoparticle/Graphene Oxide Nanocomposites and Their Excellent Catalytic Performance. *J. Mater. Chem.* **2011**, *21*, 11080–11083.

(29) Rajagopalan B.; Chung, J. S. Reduced Chemically Modified Graphene Oxide for Supercapacitor Electrode. *Nanoscale Res. Lett.* **2014**, *9*, 535.

(30) Chen, J.-L.; Yan, X.-P.; Meng, K.; Wang, S.-F. Graphene Oxide Based Photoinduced Charge Transfer Label-Free Near-Infrared Fluorescent Biosensor for Dopamine. *Anal. Chem.* **2011**, *83*, 8787–8793.

(31) Zhang, J.; Yang, H.; Shen, G.; Cheng, P.; Zhang, J.; Guo, S. Reduction of Graphene Oxide via L-Ascorbic Acid. *Chem. Commun.* **2010**, *46*, 1112–1114.

(32) Li, J.; Liu, C.-Y.; Liu, Y. Au/Graphene Hydrogel: Synthesis, Characterization and its Use for Catalytic Reduction of 4-Nitrophenol. *J. Mater. Chem.* **2012**, *22*, 8426-8430.

(33) Chuang, M.-K.; Lin, S.-W.; Chen, F.-C.; Chub, C.-W.; Hsu, C.-S. Gold Nanoparticle-Decorated Graphene Oxides for Plasmonic-Enhanced Polymer Photovoltaic Devices. *Nanoscale* **2014**, *6*, 1573–1579.

(34) Kudin, K. N.; Ozbas, B.; Schniepp, H. C.; Prudhomme, R. K.; Aksay, I. A.; Car, R. Raman Spectra of Graphite Oxide and Functionalized Graphene Sheets. *Nano Lett.* **2008**, *8*, 36-41.

(35) Wang, P.; Liu, Z.-G.; Chen, X.; Meng, F.-L.; Liu, J.-H.; Huang, X.-J. UV Irradiation Synthesis of an Au–Graphene Nanocomposite with Enhanced Electrochemical Sensing Properties. *J. Mater. Chem. A* **2013**, *1*, 9189–9195.

(36) Cuenya, B. R.; Baeck, S.-H.; Jaramillo, T. F.; McFarland, E. W. Size- and Support-Dependent Electronic and Catalytic Properties of Au^0/Au^{3+} Nanoparticles Synthesized from Block Copolymer Micelles. *J. Am. Chem. Soc.* **2003**, *125*, 12928-12934.

(37) Abdolhosseinzadeh, S.; Asgharzadeh, H.; Kim, H. S. Fast and Fully-Scalable Synthesis of Reduced Graphene Oxide. *Sci. Rep.* **2015**, *5*, 10160.

(38) Mattevi, C.; Eda, G.; Agnoli, S.; Miller, S.; Mkhoyan, K. A.; Celik, O.; Mastrogiovanni, D.; Granozzi, G.; Garfunkel, E.; Chhowalla, M. Evolution of Electrical, Chemical, and

Structural Properties of Transparent and Conducting Chemically Derived Graphene Thin Films. *Adv. Funct. Mater.* **2009**, *19*, 2577-2583.

(39) Tang, X.-Z.; Li, X.; Cao, Z.; Yang, J.; Wang, H.; Pu, X.; Yu, Z.-Z. Synthesis of Graphene Decorated with Silver Nanoparticles by Simultaneous Reduction of Graphene Oxide and Silver Ions with Glucose. *Carbon* **2013**, *59*, 93-99.

(40) Du, D.; Zou, Z.; Shin, Y.; Wang, J.; Wu, H.; Engelhard, M. H.; Liu, J.; Aksay, I. A.; Lin, Y. Sensitive Immunosensor for Cancer Biomarker Based on Dual Signal Amplification Strategy of Graphene Sheets and Multienzyme Functionalized Carbon Nanospheres. *Anal. Chem.* **2010**, *82*, 2989-2995.

(41) Darain, F.; Gan, K. L.; Tjin, S. C. Antibody immobilization on to polystyrene substrate--on-chip immunoassay for horse IgG based on fluorescence. Biomed. Microdevices **2009**, *11*, 653–661.

(42) Wang, J. *Analytical electrochemistry*. Wiley-Vch, USA 272, **2006**.

(43) Bard, A. J.; Faulkner, L. R. *Electrochemical Methods Fundamentals and Applications*. John Wiley & Sons, Inc., **2001**.

(44) Brownson, D. A. C.; Banks, C. E. *The Handbook of Graphene Electrochemistry*. Springer-Verlag London Ltd., **2014**.

(45) Nicholson, R. S. Theory and Application of Cyclic Voltammetry for Measurement of Electrode Reaction Kinetics. *Anal. Chem.* **1965**, *37*, 1351-1355.

(46) Lavagnini, I.; Antiochia R.; Magno, F. An Extended Method for the Practical Evaluation of the Standard Rate Constant from Cyclic Voltammetric Data. *Electroanalysis* **2004**, *16*, 505-506.

(47) Li, Y.; Zhang, Y.; Jiang, L.; Chu, P. K.; Dong, Y.; Wei, Q. A Sandwich-Type Electrochemical Immunosensor Based on the Biotin-Streptavidin-Biotin Structure for Detection of Human Immunoglobulin G. *Sci. Rep.* **2016**, *6*, 22694.

(48) Saha, K.; Agasti, S. S.; Kim, C.; Li, X.; Rotello, V. M. Gold Nanoparticles in Chemical and Biological Sensing. *Chem. Rev.* **2012**, *112*, 2739−2779.

(49) Hassfurther, R. L.; Canning, P. C.; Geib, R. W. Isolation and Characterization of an Interleukin-8-Like Peptide in the Bovine Species. *Vet. Immunol. Immunopathol.* **1994**, *42*, 117-126.

(50) Kumar , S.; Kumar , S.; Tiwari , S.; Srivastava , S.; Srivastava , M.; Yadav, B. K.; Kumar, S.; Tran, T. T.; Dewan, A. K.; Mulchandani, A.; Sharma, J. G.; Maji, S.; Malhotra, B. D. Biofunctionalized Nanostructured Zirconia for Biomedical Application: A Smart Approach for Oral Cancer Detection. *Adv. Sci.* **2015**, *2*, 1500048.

(51) Li, J.; Liu, S.; Yu, J.; Lian, W.; Cui, M.; Xu, W.; Huang, J. Electrochemical Immunosensor Based on Graphene-Polyaniline Composites and Carboxylated Graphene Oxide for Estradiol Detection. *Sens. Actuators, B* **2013**, *188*, 99-105.

(52) Brown, A. P.; Anson, F. C. Cyclic and Differential Pulse Voltammetric Behavior of Reactants Confined to the Electrode Surface. *Anal. Chem.* **1977**, *49*, 1589–1595.

(53) Yang, C.-Y.; Brooks, E.; Li, Y.; Denny, P.; Ho, C.-M.; Qi, F.; Shi, W.; Wolinsky, L.; Wu, B.; Wong, D. T. W.; Montemagno, C. D. Detection of Picomolar Levels of Interleukin-8 in Human Saliva by SPR. *Lab Chip* **2005**, *5*, 1017–1023.

(54) Tan, W.; Sabet, L.; Li, Y.; Yu, T.; Klokkevold, P. R.; Wong, D. T.; Ho, C.-M. Optical Protein Sensor for Detecting Cancer Markers in Saliva. *Biosens. Bioelectron.* **2008**, *24*, 266–271.

(55) Malhotra, R.; Patel, V.; Vaque´, J. P.; Gutkind, J. S.; Rusling, J. F. Ultrasensitive Electrochemical Immunosensor for Oral Cancer Biomarker IL-6 Using Carbon Nanotube Forest Electrodes and Multilabel Amplification. *Anal. Chem.* **2010**, *82*, 3118–3123.

(56) Chen, J.H.; Zhang, J.; Guo, Y.; Li, J.; Fu, F. F.; Yang, H.-H.; Chen, G. An Ultrasensitive Electrochemical Biosensor for Detection of DNA Species Related to Oral Cancer Based on Nuclease-Assisted Target Recycling and Amplification of DNAzyme. *Chem. Comm.* **2011**, *47*, 8004–8006.

(57) Munge, B. S.; Coffey, A. L.; Doucette, J. M.; Somba, B. K.; Malhotra, R.; Patel, V.; Gutkind, J. S.; Rusling, J. F. Nanostructured Immunosensor for Attomolar Detection of Cancer Biomarker Interleukin-8 Using Massively Labeled Superparamagnetic Particles. *Angew. Chem.* **2011**, *123*, 8061 –8064.

(58) Wang, Z. W.; Zhang, J.; Guo, Y.; Wua, X. Y.; Yang, W. J.; Xu, L. J.; Chen, J. H.; Fu, F. F. A Novel Electrically Magnetic-Controllable Electrochemical Biosensor for the Ultrasensitive and Specific Detection of Attomolar Level Oral Cancer-Related Micro RNA. *Biosens. Bioelectron.* **2013**, *45*, 108–113.

(59) Tan, Y.; Wei, X.; Zhao, M.; Qiu, B.; Guo, L.; Lin, Z.; Yang, H.-H. Ultraselective Homogeneous Electrochemical Biosensor for DNA Species Related to Oral Cancer Based on Nicking Endonuclease Assisted Target Recycling Amplification. *Anal. Chem.* **2015**, *87*, 9204−9208.

(60) Choudhary, M.; Yadav, P.; Singh, A.; Kaur, S.; Ramirez-Vick, J.; Chandra, P.; Arora, K.; Singh, S. P. CD 59 Targeted Ultrasensitive Electrochemical Immunosensor for Fast and Noninvasive Diagnosis of Oral Cancer. *Electroanalysis* **2016**, *28*, 1 – 11.

(61) Torrente-Rodríguez, R. M.; Campuzano, S.; Ruiz-Valdepeñas Montiel, V.; Gamella, M.; Pingarrón, J. M. Electrochemical Bioplatforms for the Simultaneous Determination of Interleukin (IL)-8 mRNA and IL-8 Protein Oral Cancer Biomarkers in Raw Saliva. *Biosens. Bioelectron.* **2016**, *77*, 543–548.

Table of Contents Figure